Journal of Sound and Vibration (2002) **249**(1), 147–164
doi:10.1006/jsvi.2001.3856, available online at http://www.idealibrary.com on IDEAL®

DYNAMIC ANALYSIS OF A ROTATING CANTILEVER BEAM BY USING THE FINITE ELEMENT METHOD

J. CHUNG

Department of Mechanical Engineering, Hanyang University, 1271 *Sa*-1-*dong*, *Ansan*, *Kyunggi-do* 425-791, *Republic of Korea. E-mail*: *jchung@hanyang.ac.kr*

AND

H. H. YOO

School of Mechanical Engineering, Hanyang University, 17 *Haengdang-dong*, *Seongdong-ku*, *Seoul* 133-791, *Republic of Korea*

(*Received* 3 *October* 2000, *and in final form* 3 *July* 2001)

A finite element analysis for a rotating cantilever beam is presented in this study. Based on a dynamic modelling method using the stretch deformation instead of the conventional axial deformation, three linear partial differential equations are derived from Hamilton's principle. Two of the linear differential equations are coupled through the stretch and chordwise deformations. The other equation is an uncoupled one for the flapwise deformation. From these partial differential equations and the associated boundary conditions, are derived two weak forms: one is for the chordwise motion and the other is for the flapwise motion. The weak forms are spatially discretized with newly defined two-node beam elements. With the discretized equations, the behaviours of the natural frequencies are investigated for the variation of the rotating speed. In addition, the time responses and distributions of the deformations and stresses are computed when the rotating speed is prescribed. The effects of the rotating speed profile on the vibrations of the beam are also investigated.

1. INTRODUCTION

Rotating cantilever beams are found in several practical engineering examples such as turbine blades and aircraft rotary wings. For reliable and economic designs of the structures, it is necessary to estimate the dynamic characteristics of those structures accurately and efficiently. Since significant variations of dynamic characteristics result from rotational motion of the structures, they have been investigated for many years.

An early analytical model to calculate natural frequencies of a rotating cantilever beam was suggested by Southwell and Gough [1]. Based on the Rayleigh energy theorem, a simple equation that relates the natural frequency to the rotating frequency of a beam was suggested. This equation is known as the Southwell equation, and widely used by many engineers nowadays. Later, to obtain more accurate natural frequencies, a linear partial differential equation that governs bending vibration of a rotating beam was derived by Schilhansl [2]. Applying the Ritz method to the equation, more accurate coefficients for the Southwell equation could be obtained. Since the early 1970s, due to the progress of computing technologies, a large number of papers based on numerical approaches have

0022-460X/02/010147 + 18 $35.00/0

been published. For instance, in references [3, 4], approximation methods for the modal analysis of rotating beams were employed. More complex shapes and the effects of beams were also considered. The effects of tip mass [5, 6], elastic foundation and cross-sectional variation [7], shear deformation [8], pre-twist and orientation of a blade [9], and gyroscopic damping effect [10] on the modal characteristics of rotating cantilever beams were studied. Survey papers for the vibration analysis of rotating structures are available [11, 12].

The most widely used modelling method for the transient analysis of structures is the classical linear modelling method [13–15]. This modelling method employs the Cartesian deformation variables and the linear Cauchy strain measures. It has several merits such as simplicity of formulation, ease of implementation in finite elements methods, and efficiency of computation which results from the use of co-ordinate reduction techniques [16, 17]. This modelling method, however, often provides erroneous results when structures undergo overall motion such as rotation. To resolve the problem of the classical linear modelling method, several non-linear modelling methods [18–20] have been developed. With these non-linear modelling methods, the problem of accuracy can be resolved. However, serious computational inefficiency results from the non-linearity that disables the co-ordinate reduction techniques. More recently, a new linear modelling method for the dynamic analysis of a flexible beam undergoing overall motion was introduced [21]. This modelling method employs hybrid deformation variables (including a stretch variable) along with a special linear strain measure. With this method, not only the accuracy problem of the classical linear modelling method but also the inefficiency of non-linear modelling methods could be resolved. However, since this modelling method employs the assumed mode method, the comparison functions should be selected as the basis function. In a situation, where the comparison functions are not available, the assumed mode method cannot be applied. To overcome this problem, it is necessary to develop a finite element analysis, based on the new modelling method, which requires only admissible functions instead of the comparison functions.

In this study, vibration and transient analysis of rotating cantilever beams are studied using the finite element method. For the purpose, the linear partial differential equations are derived for a rotating cantilever beam by Hamilton's principle. During the derivation, the chordwise and flapwise deformations as well as the stretch deformation are employed to describe the motion of the cantilever beam. From the partial differential equations and the associated boundary conditions, the weak forms are derived for the chordwise and flapwise motions. After the weak forms are spatially discretized with two-node beam elements which are defined in this paper, a set of ordinary differential equations are obtained for the chordwise and flapwise motions respectively. Based on the ordinary differential equations, the behaviours of the natural frequencies are investigated for the variation of the rotating speed. Furthermore, the transient responses and distributions of the deformations and the stresses are computed by the generalized-α method [22] when the rotating speed is prescribed. The effects of the rotating speed profile on the vibrations of the beam are also investigated.

2. EQUATIONS OF MOTION

Consider a cantilever beam of a length L, which is fixed at point O of a rigid hub with a radius a, as shown in Figure 1. The beam is modelled as the Euler–Bernoulli beam and it has homogeneous, uniform and isotropic material properties along the beam. The hub is rotating about the axis of symmetry with a rotating speed Ω. In Figure 1, the straight and

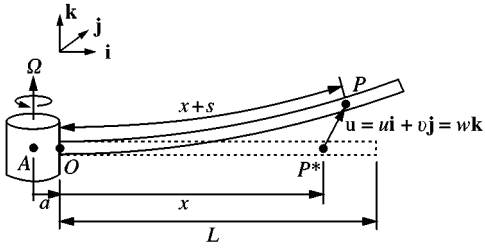

Figure 1. Configuration of a rotating cantilever beam.

curved beams represent the beams before and after deformation. The orthogonal unit vectors **i**, **j** and **k** are rotating with the hub: **i** is along the beam before deformation, **j** is in the tangential direction of the hub, and **k** is in the direction of the hub axis. Using the Cartesian co-ordinates, the deformations of the beam in the directions of **i**, **j** and **k** are generally described by the axial deformation u, the chordwise deformation v and the flapwise deformation w, respectively, when point P^* moves to point P.

As mentioned in section 1, use of the stretch deformation s has an advantage over use of the axial deformation u. According to reference [21], u is related to s, v and w:

$$u = s - h_v - h_w, \tag{1}$$

where

$$h_v = \frac{1}{2}\int_0^x \left(\frac{\partial v}{\partial \eta}\right)^2 \mathrm{d}\eta, \quad h_w = \frac{1}{2}\int_0^x \left(\frac{\partial w}{\partial \eta}\right)^2 \mathrm{d}\eta \tag{2}$$

in which η is a dummy variable. Similarly, the time derivative of u is given by

$$\dot{u} = \dot{s} - \dot{h}_v - \dot{h}_w, \tag{3}$$

where the superposed dots indicate the derivative with respect to time, and

$$\dot{h}_v = \int_0^x \frac{\partial v}{\partial \eta}\frac{\partial \dot{v}}{\partial \eta}\mathrm{d}\eta, \quad \dot{h}_w = \int_0^x \frac{\partial w}{\partial \eta}\frac{\partial \dot{w}}{\partial \eta}\mathrm{d}\eta. \tag{4}$$

The kinetic and strain energies of the rotating cantilever beam can be expressed in terms of the stretch, chordwise and flapwise deformations. When the cantilever beam is rotating with Ω, the kinetic energy of the beam is given by

$$T = \frac{1}{2}\rho A \int_0^L \mathbf{v}_P \cdot \mathbf{v}_P \,\mathrm{d}x, \tag{5}$$

where ρ and A are the mass density and cross-sectional area of the beam; $\mathbf{v}_P$ is the velocity vector of a particle at point P:

$$\mathbf{v}_P = (\dot{u} - \Omega v)\mathbf{i} + [\dot{v} + \Omega(a + x + u)]\mathbf{j} + \dot{w}\mathbf{k}. \tag{6}$$

Substitution of equation (6) into equation (5) after introducing equations (1) and (3) to equation (6) leads to

$$T = \frac{1}{2}\rho A \int_0^L \{[\dot{s} - \Omega v - (\dot{h}_v + \dot{h}_w)]^2 + [\dot{v} + \Omega(a + x + s) - \Omega(h_v + h_w)]^2 + \dot{w}^2\}\,\mathrm{d}x. \tag{7}$$

On the other hand, the strain energy for the beam can be expressed as

$$U = \frac{1}{2} E \int_0^L \left[A\left(\frac{\partial s}{\partial x}\right)^2 + I_z\left(\frac{\partial^2 v}{\partial x^2}\right)^2 + I_y\left(\frac{\partial^2 w}{\partial x^2}\right)^2 \right] \mathrm{d}x, \tag{8}$$

where E is Young's modulus; I_y and I_z are the area moments of inertia about the y- and z- axes respectively. For simplicity, this study assumes that E, A, I_y and I_z are constant along the beam, i.e., independent of x.

The equations of motion are derived by applying Hamilton's principle, which is given by

$$\int_{t_1}^{t_2} \int_0^L \delta \mathscr{L}\,\mathrm{d}x\,\mathrm{d}t = 0, \tag{9}$$

where t_1 and t_2 are arbitrary time and $\mathscr{L}$ is the Lagrangian density function

$$\begin{aligned} \mathscr{L} = {} & \frac{1}{2}\rho A \{[\dot{s} - \Omega v - (\dot{h}_v + \dot{h}_w)]^2 + [\dot{v} + \Omega(a + x + s) - \Omega(h_v + h_w)]^2 + \dot{w}^2\} \\ & - \frac{1}{2} E \left[A\left(\frac{\partial s}{\partial x}\right)^2 + I_z\left(\frac{\partial^2 v}{\partial x^2}\right)^2 + I_y\left(\frac{\partial^2 w}{\partial x^2}\right)^2 \right]. \end{aligned} \tag{10}$$

Taking the variation of the Lagrangian density function, integrating equation (9) by parts, and then collecting all the terms of the integrand with respect to δs, δv and δw, the coefficients of δs, δv and δw result in the following equations of motion:

$$\rho A \left[\frac{\partial^2 s}{\partial t^2} - 2\Omega \frac{\partial v}{\partial t} - \Omega^2 s - \dot{\Omega} v + \Omega^2 (h_v + h_w) - \frac{\partial^2}{\partial t^2}(h_v + h_w) \right] - EA \frac{\partial^2 s}{\partial x^2} = \rho A \Omega^2 (a + x), \tag{11}$$

$$\begin{aligned} & \rho A \left[\frac{\partial^2 v}{\partial t^2} + 2\Omega \frac{\partial s}{\partial t} - \Omega^2 v + \dot{\Omega} s - 2\Omega \frac{\partial}{\partial t}(h_v + h_w) - \dot{\Omega}(h_v + h_w) \right] + EI_z \frac{\partial^4 v}{\partial x^4} \\ & - \frac{\partial}{\partial x} \left\{ \frac{\partial v}{\partial x} \int_L^x \rho A \left[\frac{\partial^2 s}{\partial t^2} - 2\Omega \frac{\partial v}{\partial t} - \Omega^2 (a + \xi + s) - \dot{\Omega} v + \Omega^2 (h_v + h_w) - \frac{\partial^2}{\partial t^2}(h_v + h_w) \right] \mathrm{d}\xi \right\} \\ & = -\rho A \dot{\Omega}(a + x), \end{aligned} \tag{12}$$

$$\begin{aligned} & \rho A \frac{\partial^2 w}{\partial t^2} + EI_y \frac{\partial^4 w}{\partial x^4} \\ & - \frac{\partial}{\partial x} \left\{ \frac{\partial w}{\partial x} \int_L^x \rho A \left[\frac{\partial^2 s}{\partial t^2} - 2\Omega \frac{\partial v}{\partial t} - \Omega^2 (a + \xi + s) - \dot{\Omega} v + \Omega^2 (h_v + h_w) - \frac{\partial^2}{\partial t^2}(h_v + h_w) \right] \mathrm{d}\xi \right\} = 0. \end{aligned} \tag{13}$$

Note that equations (11)–(13) are non-linear partial differential equations. Consideration of the non-conservative applied forces in the y and z directions and linearization of the

non-linear equations yield the following linear partial differential equations:

$$\rho A\left(\frac{\partial^2 s}{\partial t^2} - 2\Omega\frac{\partial v}{\partial t} - \Omega^2 s - \dot{\Omega}v\right) - EA\frac{\partial^2 s}{\partial x^2} = \rho A\Omega^2(a+x), \tag{14}$$

$$\rho A\left(\frac{\partial^2 v}{\partial t^2} + 2\Omega\frac{\partial s}{\partial t} - \Omega^2 v + \dot{\Omega}s\right) + EI_z\frac{\partial^4 v}{\partial x^4} - \rho A\Omega^2\frac{\partial}{\partial x}\left\{\left[a(L-x) + \frac{1}{2}(L^2 - x^2)\right]\frac{\partial v}{\partial x}\right\} = p_v - \rho A\dot{\Omega}(a+x), \tag{15}$$

$$\rho A\frac{\partial^2 w}{\partial t^2} + EI_y\frac{\partial^4 w}{\partial x^4} - \rho A\Omega^2\frac{\partial}{\partial x}\left\{\left[a(L-x) + \frac{1}{2}(L^2 - x^2)\right]\frac{\partial w}{\partial x}\right\} = p_w. \tag{16}$$

where p_v and p_w are the applied forces per unit length in the y and z directions. It is interesting that equations (14) and (15) are coupled with each other while equation (16) is not coupled with the other equations. In this paper, a motion described by equations (14) and (15) is called the chordwise motion, and a motion described by equation (16) is called the flapwise motion. The boundary conditions corresponding to equations (14)–(16) are given by

$$s = v = w = \frac{\partial v}{\partial x} = \frac{\partial w}{\partial x} = 0 \quad \text{at } x = 0, \tag{17}$$

$$\frac{\partial s}{\partial x} = \frac{\partial^2 v}{\partial x^2} = \frac{\partial^2 w}{\partial x^2} = \frac{\partial^3 v}{\partial x^3} = \frac{\partial^3 w}{\partial x^3} = 0 \quad \text{at } x = L. \tag{18}$$

Equation (17) is for the essential or geometric boundary conditions and equation (18) is for the natural boundary conditions. In addition, the initial conditions may be imposed by equations (14)–(16).

3. FINITE ELEMENT ANALYSIS

The partial differential equations given by equations (14)–(16) are solved by the finite element method in this study. From the partial differential equations and the boundary conditions, the weak forms or the variational forms are derived. Spatial discretization of the weak forms leads to the initial value problems, which are constituted by systems of the ordinary differential equations and the corresponding initial conditions. When time histories of responses are required, the time integration is applied to the initial value problems. However, if the dynamic characteristics of a given system are required, the eigenvalue problems are deduced from the ordinary differential equations.

Before derivation of the weak forms, it is necessary to define the trial and weighting functions. In one-dimensional problems, the Hilbert space, H^1, is defined as

$$H^1 = \left\{ v \,|\, v \text{ is continuous on } [0, L],\ \partial v/\partial x \text{ is piecewise continuous, and } \int_0^L (\partial v/\partial x)^2\,\mathrm{d}x < \infty \right\}. \tag{19}$$

Equation (19) means that the strain energy of a system is bounded if a solution is represented by a function in the Hilbert space. The trial function is defined as a function in the Hilbert space H^1, satisfying all the boundary conditions, namely, both the essential and natural boundary conditions. This means that the trial function is a sort of the comparison function. The trial functions for the stretch, chordwise and flapwise deformations, related to equations (14)–(18), can be defined as follows:

$$s \in V_s = \{s \,|\, s \in H^1, \quad s(0) = \partial s/\partial x|_{x=L} = 0\}, \tag{20}$$

$$v, w \in V_{vw} = \{v \,|\, v \in H^1, \partial v/\partial x \in H^1, v(0) = \partial v/\partial x|_{x=0} = \partial^2 v/\partial x^2|_{x=L} = \partial^3 v/\partial x^3|_{x=L} = 0\}, \tag{21}$$

where V_s is the trial function space for the stretch deformation and V_{vw} are the ones for the chordwise and flapwise deformations. Equation (21) implies that not only the deformations v and w but also their derivatives should be in the Hilbert space. This is because the slopes as well as the deformations should be described as degrees of freedom in the beam theory of the finite element method. On the other hand, the weighting function is defined as a function in the H^1 space, which should be zero on the boundaries where the essential boundary conditions are prescribed. Hence, the weighting functions for the stretch, chordwise and flapwise deformations are defined by

$$\bar{s} \in \bar{V}_s = \{\bar{s} \,|\, \bar{s} \in H^1, \bar{s}(0) = 0\}, \tag{22}$$

$$\bar{v}, \bar{w} \in \bar{V}_{vw} = \{\bar{v} \,|\, \bar{v} \in H^1, \partial \bar{v}/\partial x \in H^1, \bar{v}(0) = \partial \bar{v}/\partial x|_{x=0} = 0\}. \tag{23}$$

The weak forms need to be derived from the strong forms given by the partial differential equations and the corresponding boundary conditions. Since equations (14) and (15) are coupled equations but equation (16) is not a coupled one, this study derives two weak forms: a weak form for the chordwise motion and a weak form for the flapwise motion. The weak form for the chordwise motion is obtained by multiplying equations (14) and (15) by the weighting functions $\bar{s}$ and $\bar{v}$, respectively, summing the equations, and then integrating the resultant equation by parts over the length L. The weak form for the chordwise motion can be expressed as

$$\begin{aligned} &\rho A \int_0^L \left[\bar{s} \left(\frac{\partial^2 s}{\partial t^2} - 2\Omega \frac{\partial v}{\partial t} - \Omega^2 s - \dot{\Omega} v \right) + \bar{v} \left(\frac{\partial^2 v}{\partial t^2} + 2\Omega \frac{\partial s}{\partial t} - \Omega^2 v + \dot{\Omega} s \right) \right] \mathrm{d}x \\ &\quad + \int_0^L \left(EA \frac{\partial \bar{s}}{\partial x} \frac{\partial s}{\partial x} + EI_z \frac{\partial^2 \bar{v}}{\partial x^2} \frac{\partial^2 v}{\partial x^2} \right) \mathrm{d}x + \rho A \Omega^2 \int_0^L \left[a(L-x) + \frac{1}{2}(L^2 - x^2) \right] \frac{\partial \bar{v}}{\partial x} \frac{\partial v}{\partial x} \mathrm{d}x \\ &\quad = \int_0^L \{ \rho A \Omega^2 (a + x) \bar{s} + [p_v - \rho A \dot{\Omega} (a + x)] \bar{v} \} \, \mathrm{d}x. \end{aligned} \tag{24}$$

In a similar manner, the weak form for the flapwise motion is derived by multiplying equation (16) by the weighting function $\bar{w}$ and then integrating the equation by parts:

$$\begin{aligned} &\rho A \int_0^L \bar{w} \frac{\partial^2 w}{\partial t^2} \, \mathrm{d}x + EI_y \int_0^L \frac{\partial^2 \bar{w}}{\partial x^2} \frac{\partial^2 w}{\partial x^2} \, \mathrm{d}x + \rho A \Omega^2 \int_0^L \left[a(L-x) + \frac{1}{2}(L^2 - x^2) \right] \frac{\partial \bar{w}}{\partial x} \frac{\partial w}{\partial x} \, \mathrm{d}x \\ &\quad = \int_0^L \bar{w} p_w \, \mathrm{d}x. \end{aligned} \tag{25}$$

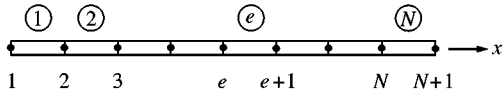

Figure 2. Element and node numbers of a finite element model.

It is noted that the natural boundary conditions given by equation (18) are satisfied by the above weak forms.

Next, consider the local description of the deformations in an element. In this study the cantilever beam is discretized into N two-node elements as shown in Figure 2, where the numbers above and below the beam represent the element and node numbers respectively. In element e defined by node numbers e and $e+1$, the stretch, chordwise and flapwise deformations can be approximated as linear or cubic polynomials:

$$s = a_1 + a_2 x, \quad v = a_3 + a_4 x + a_5 x^2 + a_6 x^3, \quad w = a_7 + a_8 x + a_9 x^2 + a_{10} x^3, \tag{26}$$

where a_i's are coefficients to be determined by the deformations and corresponding slopes at the nodes. Denote the stretch deformation at node e by s_e, the chordwise and flapwise deformations by v_e and w_e, and the chordwise and flapwise slopes by, θ_e and ψ_e:

$$s(x_e) = s_e, \quad v(x_e) = v_e, \quad w(x_e) = w_e, \quad \partial v/\partial x|_{x=x_e} = \theta_e, \quad \partial w/\partial x|_{x=x_e} = \psi_e. \tag{27}$$

From equations (26) and (27), the stretch, chordwise and flapwise deformations at an arbitrary point in element e can be expressed in terms of those at the nodes. Hence, equation (26) may be rewritten as

$$s = \mathbf{N}_s^{\mathrm{T}} \mathbf{d}_e^{sv}, \quad v = \mathbf{N}_v^{\mathrm{T}} \mathbf{d}_e^{sv}, \quad w = \mathbf{N}_w^{\mathrm{T}} \mathbf{d}_e^{w}, \tag{28}$$

where $\mathbf{d}_e^{sv}$ and $\mathbf{d}_e^{w}$ are the element deformation vectors; $\mathbf{N}_s$, $\mathbf{N}_v$ and $\mathbf{N}_w$ are the shape function vectors:

$$\mathbf{d}_e^{sv} = \{s_e, v_e, \theta_e, s_{e+1}, v_{e+1}, \theta_{e+1}\}^{\mathrm{T}}, \quad \mathbf{d}_e^{w} = \{w_e, \psi_e, w_{e+1}, \psi_{e+1}\}^{\mathrm{T}}, \tag{29}$$

$$\begin{aligned}
\mathbf{N}_s &= \{(x_{e+1} - x)/h_e, 0, 0, (x - x_e)/h_e, 0, 0\}^{\mathrm{T}}, \\
\mathbf{N}_v &= \{0, (x - x_{e+1})^2(2x - 3x_e + x_{e+1})/h_e^3, (x - x_e)(x - x_{e+1})^2/h_e^2, \\
&\quad 0, -(x - x_e)^2(2x + x_e - 3x_{e+1})/h_e^3, (x - x_e)^2(x - x_{e+1})/h_e^2\}^{\mathrm{T}}, \\
\mathbf{N}_w &= \{(x - x_{e+1})^2(2x - 3x_e + x_{e+1})/h_e^3, (x - x_e)(x - x_{e+1})^2/h_e^2, \\
&\quad -(x - x_e)^2(2x + x_e - 3x_{e+1})/h_e^3, (x - x_e)^2(x - x_{e+1})/h_e^2\}^{\mathrm{T}}
\end{aligned} \tag{30}$$

in which h_e is the element size given by

$$h_e = x_{e+1} - x_e. \tag{31}$$

Equation (28) implies that the stretch and chordwise deformations are described by the degrees of freedom of $s_e, v_e, \theta_e, s_{e+1}, v_{e+1}$ and θ_{e+1}, while those for the flapwise motion are described by the degrees of freedom of w_e, ψ_e, w_{e+1} and ψ_{e+1}. Figure 3 shows finite

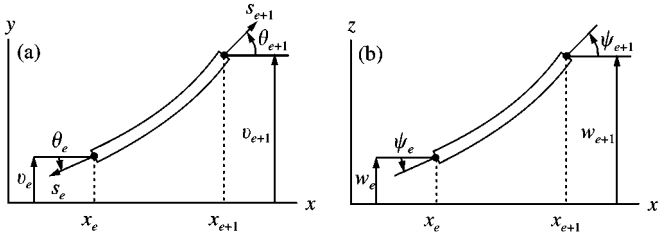

Figure 3. Finite elements for (a) the chordwise motion and (b) the flapwise motion.

elements for the chordwise and flapwise motions. On the other hand, the weighting functions for the stretch, chordwise and flapwise deformations are given by

$$\bar{s} = (\boldsymbol{\eta}_e^{sv})^{\mathrm{T}}\mathbf{N}_s, \quad \bar{v} = (\boldsymbol{\eta}_e^{sv})^{\mathrm{T}}\mathbf{N}_v, \quad \bar{w} = (\boldsymbol{\eta}_e^{w})^{\mathrm{T}}\mathbf{N}_w, \tag{32}$$

where $\boldsymbol{\eta}_e^{sv}$ and $\boldsymbol{\eta}_e^{w}$ are arbitrary 6×1 and 4×1 column vectors respectively.

A solution of the finite element method, that is, an approximate solution, is obtained in a finite dimensional function space. In order to find approximate solutions of equations (14)–(16), the weak forms given by equations (24) and (25) are discretized by using the two-node beam elements defined above. After discretizing the domain $[0, L]$ into the subdomains $[x_e, x_{e+1}]$, $e = 1, 2, \ldots, N$, as shown in Figure 2, introduction of equations (28) and (32) to equations (24) and (25) yields discretized equations. The discretized equation for the chordwise motion is

$$\sum_{e=1}^{N} (\boldsymbol{\eta}_e^{sv})^{\mathrm{T}} \{\mathbf{m}_e^{sv}\ddot{\mathbf{d}}_e^{sv} + 2\Omega\mathbf{g}_e^{sv}\dot{\mathbf{d}}_e^{sv} + [\mathbf{k}_e^{sv} + \Omega^2(\mathbf{s}_e^{sv} - \mathbf{m}_e^{sv}) + \dot{\Omega}\mathbf{g}_e^{sv}]\mathbf{d}_e^{sv}\} = \sum_{e=1}^{N} (\boldsymbol{\eta}_e^{sv})^{\mathrm{T}}\mathbf{f}_e^{sv}, \tag{33}$$

where $\mathbf{m}_e^{sv}$, $\mathbf{g}_e^{sv}$, $\mathbf{k}_e^{sv}$ and $\mathbf{s}_e^{sv}$ are the element mass, the element gyroscopic, the element stiffness and the element motion-induced stiffness matrices for the chordwise motion; $\mathbf{f}_e^{sv}$ is the element load vector for the chordwise motion. These element matrices and vector may be expressed as

$$\mathbf{m}_e^{sv} = \rho A \int_{x_e}^{x_{e+1}} (\mathbf{N}_s\mathbf{N}_s^{\mathrm{T}} + \mathbf{N}_v\mathbf{N}_v^{\mathrm{T}})\,\mathrm{d}x, \quad \mathbf{g}_e^{sv} = \rho A \int_{x_e}^{x_{e+1}} (\mathbf{N}_v\mathbf{N}_s^{\mathrm{T}} - \mathbf{N}_s\mathbf{N}_v^{\mathrm{T}})\,\mathrm{d}x,$$

$$\mathbf{k}_e^{sv} = \int_{x_e}^{x_{e+1}} \left(EA\frac{\mathrm{d}\mathbf{N}_s}{\mathrm{d}x}\frac{\mathrm{d}\mathbf{N}_s^{\mathrm{T}}}{\mathrm{d}x} + EI_z\frac{\mathrm{d}^2\mathbf{N}_v}{\mathrm{d}x^2}\frac{\mathrm{d}^2\mathbf{N}_v^{\mathrm{T}}}{\mathrm{d}x^2}\right)\mathrm{d}x,$$

$$\mathbf{s}_e^{sv} = \rho A \int_{x_e}^{x_{e+1}} \left[a(L-x) + \frac{1}{2}(L^2 - x^2)\right]\frac{\mathrm{d}\mathbf{N}_v}{\mathrm{d}x}\frac{\mathrm{d}\mathbf{N}_v^{\mathrm{T}}}{\mathrm{d}x}\,\mathrm{d}x,$$

$$\mathbf{f}_e^{sv} = \int_{x_e}^{x_{e+1}} \{\rho A\Omega^2(a+x)\mathbf{N}_s + [p_v - \rho A\dot{\Omega}(a+x)]\mathbf{N}_v\}\,\mathrm{d}x. \tag{34}$$

In the same way, the discretized equation for the flapwise motion are given by

$$\sum_{e=1}^{N} (\boldsymbol{\eta}_e^{w})^{\mathrm{T}} [\mathbf{m}_e^{w}\ddot{\mathbf{d}}_e^{w} + (\mathbf{k}_e^{w} + \Omega^2\mathbf{s}_e^{w})\mathbf{d}_e^{w}] = \sum_{e=1}^{N} (\boldsymbol{\eta}_e^{w})^{\mathrm{T}}\mathbf{f}_e^{w}, \tag{35}$$

where $\mathbf{m}_e^w$, $\mathbf{k}_e^w$ and $\mathbf{s}_e^w$ are the element mass, the element stiffness and the element motion-induced stiffness matrices for the flapwise motion and $\mathbf{f}_e^w$ is the element load vector for the flapwise motion:

$$\mathbf{m}_e^w = \rho A \int_{x_e}^{x_{e+1}} \mathbf{N}_w \mathbf{N}_w^{\mathrm{T}} \, \mathrm{d}x, \quad \mathbf{k}_e^w = EI_y \int_{x_e}^{x_{e+1}} \frac{\mathrm{d}^2\mathbf{N}_w}{\mathrm{d}x^2} \frac{\mathrm{d}^2\mathbf{N}_w^{\mathrm{T}}}{\mathrm{d}x^2} \, \mathrm{d}x,$$

$$\mathbf{s}_e^w = \rho A \int_{x_e}^{x_{e+1}} \left[a(L-x) + \frac{1}{2}(L^2 - x^2) \right] \frac{\mathrm{d}\mathbf{N}_w}{\mathrm{d}x} \frac{\mathrm{d}\mathbf{N}_w^{\mathrm{T}}}{\mathrm{d}x} \, \mathrm{d}x, \quad \mathbf{f}_e^w = \int_{x_e}^{x_{e+1}} p_w \mathbf{N}_w \, \mathrm{d}x. \tag{36}$$

Since $\boldsymbol{\eta}_e^{sv}$ and $\boldsymbol{\eta}_e^w$ are arbitrary vectors, by assembling the element matrices and vectors, equations (33) and (35) can be transformed to the global equations. The global equation for the chordwise motion is given by

$$\mathbf{M}_{sv}\ddot{\mathbf{d}}_{sv} + 2\Omega\mathbf{G}_{sv}\dot{\mathbf{d}}_{sv} + [\mathbf{K}_{sv} + \Omega^2(\mathbf{S}_{sv} - \mathbf{M}_{sv}) + \dot{\Omega}\mathbf{G}_{sv}]\mathbf{d}_{sv} = \mathbf{f}_{sv}, \tag{37}$$

where $\mathbf{d}_{sv}$ is the global deformation vector for the chordwise motion; $\mathbf{M}_{sv}$, $\mathbf{G}_{sv}$, $\mathbf{K}_{sv}$ and $\mathbf{S}_{sv}$ are the global mass, the global gyroscopic, the global stiffness and the global motion-induced stiffness matrices; $\mathbf{f}_{sv}$ is the global load vector.

$$\mathbf{d}_{sv} = \{s_2, v_2, \theta_2, s_3, v_3, \theta_3, \ldots, s_{N+1}, v_{N+1}, \theta_{N+1}\}^{\mathrm{T}}, \tag{38}$$

$$\mathbf{M}_{sv} = \mathop{\mathrm{A}}_{e=1}^{N} \mathbf{m}_e^{sv}, \quad \mathbf{G}_{sv} = \mathop{\mathrm{A}}_{e=1}^{N} \mathbf{g}_e^{sv}, \quad \mathbf{K}_{sv} = \mathop{\mathrm{A}}_{e=1}^{N} \mathbf{k}_e^{sv}, \quad \mathbf{S}_{sv} = \mathop{\mathrm{A}}_{e=1}^{N} \mathbf{s}_e^{sv}, \quad \mathbf{f}_{sv} = \mathop{\mathrm{A}}_{e=1}^{N} \mathbf{f}_e^{sv} \tag{39}$$

in which $\mathbf{A}$ denotes the assembly operator. Similarly, the global equation for the flapwise motion becomes

$$\mathbf{M}_w\ddot{\mathbf{d}}_w + (\mathbf{K}_w + \Omega^2\mathbf{S}_w)\mathbf{d}_w = \mathbf{f}_w, \tag{40}$$

where $\mathbf{d}_w$ is the global deformation vector for the flapwise motion, $\mathbf{M}_w$, $\mathbf{K}_w$ and $\mathbf{S}_w$ are the global matrices, and $\mathbf{f}_w$ is the global load vector.

$$\mathbf{d}_w = \{w_2, \psi_2, w_3, \psi_3, \ldots, w_{N+1}, \psi_{N+1}\}^{\mathrm{T}}, \tag{41}$$

$$\mathbf{M}_w = \mathop{\mathrm{A}}_{e=1}^{N} \mathbf{m}_e^w, \quad \mathbf{K}_w = \mathop{\mathrm{A}}_{e=1}^{N} \mathbf{k}_e^w, \quad \mathbf{S}_w = \mathop{\mathrm{A}}_{e=1}^{N} \mathbf{s}_e^w, \quad \mathbf{f}_w = \mathop{\mathrm{A}}_{e=1}^{N} \mathbf{f}_e^w. \tag{42}$$

Since s_1, v_1, w_1, θ_1 and ψ_1 are known degrees of freedom in the cantilever model, i.e., non-active degrees of freedom, they are not involved in equations (38) and (41) that consist of active degrees of freedom.

4. NATURAL FREQUENCIES

For simplicity of numerical investigations, assume that the beam has equal area moments of inertia about the y- and z-axis, i.e., $I_y = I_z$. Furthermore, for convenience of discussions, dimensionless parameters are introduced as follows:

$$\tau = \frac{t}{T}, \quad \xi = \frac{x}{L}, \quad \delta = \frac{a}{L}, \quad \gamma = T\Omega, \quad \alpha = \sqrt{\frac{AL^2}{I_z}}, \quad \lambda = T^2\dot{\Omega}, \tag{43}$$

where

$$T = \sqrt{\frac{\rho A L^4}{EI_z}}. \tag{44}$$

From the discretized equations of motion given by equations (37) and (40), the eigenvalue problems are derived, in which the natural frequencies can be computed for the chordwise and flapwise motions. Assume the steady state solutions of equations (37) and (40) as

$$\mathbf{d}_{sv} = \mathbf{X}_{sv} e^{i\omega_{sv}\tau}, \quad \mathbf{d}_w = \mathbf{X}_w e^{i\omega_w \tau}, \tag{45}$$

where $i = \sqrt{-1}$; ω_{sv} and ω_w are the dimensionless natural frequencies for the chordwise and flapwise motions; $\mathbf{X}_{sv}$ and $\mathbf{X}_w$ are the amplitudes of vibrations. Neglecting the applied forces and the rotating acceleration, substitution of equation (45) into equations (37) and (40) leads to the eigenvalue problems given by

$$\{[\mathbf{K}_{sv} + \Omega^2(\mathbf{S}_{sv} - \mathbf{M}_{sv})] + 2i\omega_{sv}\Omega\mathbf{G}_{sv} - \omega_{sv}^2\mathbf{M}_{sv}\}\mathbf{X}_{sv} = \mathbf{0}, \tag{46}$$

$$\{(\mathbf{K}_w + \Omega^2\mathbf{S}_w) - \omega_w^2\mathbf{M}_w\}\mathbf{X}_w = \mathbf{0}. \tag{47}$$

Consider the convergence characteristics of the natural frequencies, when the beam is stationary, i.e., $\gamma = 0$ and values of δ and α are 0 and 70 respectively. A value of $\alpha = 70$ guarantees that the beam is slender enough for the Euler–Bernoulli beam theory to be applied. As shown in Table 1, the natural frequencies for the chordwise motion, which are obtained from equation (46), converge to the exact values as the number of elements increases. The convergence test, in the case of the flapwise motion, shows that the natural frequencies computed from equation (47) are identical to those of the bending modes for the chordwise motion presented in Table 1.

The proposed finite element method can be verified by comparing the natural frequencies computed from the present study and reference [10]. All of the computations below use the 100 two-node beam elements in the discretized models for the chordwise and flapwise motions. Table 2 shows that, for $\alpha = 70$ and various values of δ and γ, the first dimensionless natural frequencies for the chordwise motion computed from the present method are very

TABLE 1

Convergence characteristics of the dimensionless natural frequencies for the chordwise motion when $\delta = \gamma = 0$ *and* $\alpha = 70$

No. of elements	Bending modes				Stretching mode	
	1st	2nd	3rd	4th	1st	2nd
5	3·5161	22·0455	61·9188	122·3197	110·4085	493·2637
10	3·5160	22·0352	61·7129	121·0171	110·0688	421·1489
20	3·5160	22·0345	61·6982	120·7686	109·9840	417·2923
40	3·5160	22·0345	61·6973	120·9024	109·9628	393·0742
60	3·5160	22·0345	61·6972	120·9033	109·9590	370·6638
80	3·5160	22·0345	61·6972	120·8444	109·9576	334·9260
100	3·5160	22·0345	61·6972	120·9019	109·9569	330·8796
Exact	3·5160	22·0345	61·6972	120·9019	109·9557	329·8672

TABLE 2

Comparison of the first dimensionless natural frequencies for the chordwise motion when $\alpha = 70$

δ	γ	Present ($N = 100$)	Reference [10]
0	2	3·6196	3·6196
	10	4·9700	4·9703
	50	7·3337	7·5540
1	2	4·3978	4·3978
	10	13·0482	13·0494
	50	41·2275	41·3791
5	2	6·6430	6·6430
	10	27·2660	27·2761
	50	74·0031	74·1949

TABLE 3

Comparison of the first and second dimensionless natural frequencies for the flapwise motion when $\delta = 0$ *and* $\alpha = 70$

	First natural frequency		Second natural frequency	
γ	Present ($N = 100$)	Reference [10]	Present ($N = 100$)	Reference [10]
0	3·5160	3·5160	22·0345	22·0345
1	3·6816	3·6816	22·1810	22·1810
2	4·1373	4·1373	22·6149	22·6149
3	4·7973	4·7973	23·3203	23·3203
4	5·5850	5·5850	24·2733	24·2734
5	6·4495	6·4496	25·4461	25·4461
6	7·3604	7·3604	26·8091	26·8092
7	8·2996	8·2997	28·3341	28·3342
8	9·2568	9·2569	29·9954	29·9956
9	10·2257	10·2258	31·7705	31·7709
10	11·2023	11·2025	33·6404	33·6409

close to those in reference [10]. Furthermore, the first and second natural frequencies for the flapwise motion are compared between the present study and reference [10] when $\delta = 0$ and $\alpha = 70$. This comparison for various values of γ is presented in Table 3, in which the dimensionless natural frequencies computed by the two methods agree well with each other.

It is interesting to investigate the behaviours of the natural frequencies for variation of the rotating speed. Figure 4 demonstrates the variation of the dimensionless natural frequencies for the dimensionless rotating speed, when $\lambda = 0$, $\delta = 0.1$ and $\alpha = 70$. In the curves of the natural frequencies versus the rotating speed, the main differences between the chordwise and flapwise motions are the presence of the stretching modes and the occurrence of the divergence instability. As shown in Figure 4(b), the natural frequencies of the flapwise bending motion monotonically increase with the rotating speed. However, Figure 4(a) illustrates that in the chordwise motion the stretching modes denoted by S1 and S2 are

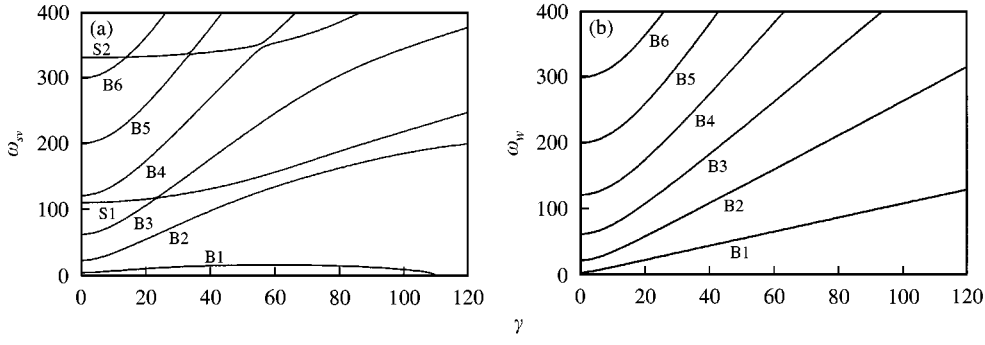

Figure 4. Variation of the dimensionless natural frequencies for the dimensionless rotating speed γ when $\lambda = 0$, $\delta = 0{\cdot}1$ and $\alpha = 70$: (a) the chordwise motion; and (b) the flapwise motion.

coupled with the bending modes denoted by B1, B2 and so on. This coupling effect between the stretching and bending modes results in the well-known veering phenomena shown in Figure 4(a), where it is observed that two natural frequency loci veer rather than cross. For instance, S1 and B3 veer at $\gamma = 23{\cdot}4$, S2 and B6 do at $\gamma = 13{\cdot}8$, and B6 and B5 do at $\gamma = 33{\cdot}0$. As the angular speed increases, the associated mode shapes change abruptly around the veering region [10]. It is also observed that the natural frequency of the first chordwise bending mode denoted B1 becomes zero at a specific rotating speed. This speed is the critical speed for the divergence instability of the rotating beam.

5. TIME RESPONSES

In this section, time responses for a rotating beam with $\delta = 0{\cdot}1$ and $\alpha = 70$ are computed using the generalized-α method [22], when the rotating speed is prescribed. The finite element model has the 100 two-node beam elements. This study considers two types of rotating speed profiles: the smooth profile and the non-smooth profile. The smooth speed profile is given by

$$\gamma = \begin{cases} \tau - \dfrac{5}{\pi}\sin\dfrac{\pi\tau}{5} & \text{if } 0 \leqslant \tau \leqslant 10, \\ 10 & \text{if } 10 \leqslant \tau \leqslant 40, \\ 50 - \tau + \dfrac{5}{\pi}\sin\dfrac{\pi\tau}{5} & \text{if } 40 \leqslant \tau \leqslant 50 \end{cases} \tag{48}$$

while the non-smooth speed profile is given by

$$\gamma = \begin{cases} \tau & \text{if } 0 \leqslant \tau \leqslant 10, \\ 10 & \text{if } 10 \leqslant \tau \leqslant 40, \\ 50 - \tau & \text{if } 40 \leqslant \tau \leqslant 50. \end{cases} \tag{49}$$

These dimensionless rotating speed profiles are plotted in Figure 5. The zero initial conditions are imposed on the chordwise and flapwise motions:

$$\mathbf{d}_{sv}(0) = \mathbf{d}_w(0) = \mathbf{0}, \quad \dot{\mathbf{d}}_{sv}(0) = \dot{\mathbf{d}}_w(0) = \mathbf{0}. \tag{50}$$

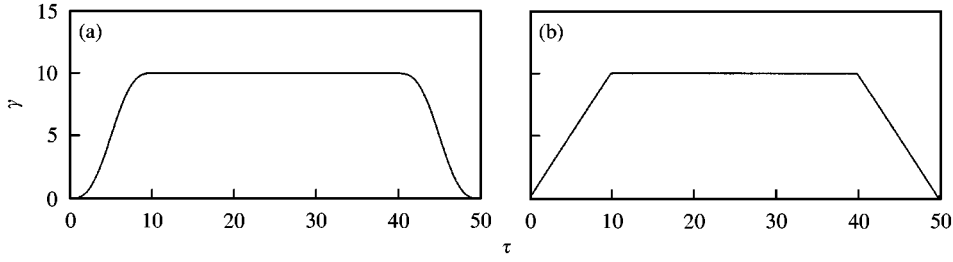

Figure 5. Profiles of the dimensionless rotating speed γ for the dimensionless time τ: (a) the smooth profile and (b) the non-smooth profile.

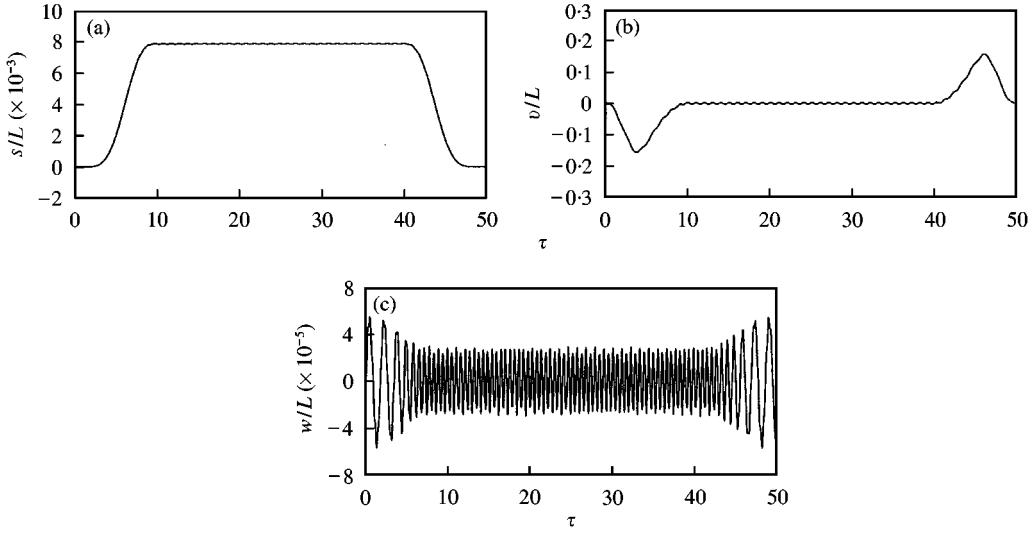

Figure 6. Deformation time histories at $\xi = 1$ for the smooth rotating speed profile: (a) the dimensionless stretch deformation s/L; (b) the dimensionless chordwise deformation v/L; and (c) the dimensionless flapwise deformation w/L.

Furthermore, assume that no force is applied in the chordwise direction but the unit impulsive pressure is applied in the flapwise direction.

Time histories of the deformations at the free end, i.e., at $\xi = 1$ are computed when the rotating speed is prescribed. Figures 6 and 7 show the time histories of the deformation for the smooth and non-smooth profiles respectively. Note that the non-smooth speed profile incurs larger vibration in the chordwise motion than the smooth one. Since the non-smooth speed profile yields a discontinuous rotating acceleration, the profile is equivalent to a sudden change in the applied load. Therefore, when the beam rotates with the smooth speed profile, a large amount of vibration is reduced. On the other hand, when, at the initial time, the unit impulsive pressure is applied to the rotating beam in the flapwise direction, the amplitude of the flapwise vibration is influenced by the rotating speed. Figures 6(c) and 7(c) illustrate that the amplitude of the flapwise vibration decreases, remains constant and then increases, as the rotating speed increases, remains constant and decreases. It is also observed that the period of vibration seems to be inversely proportional to the rotating speed. Note that the smoothness of the rotating speed profile makes no significant difference in the flapwise deformations, as shown in Figures 6(c) and 7(c).

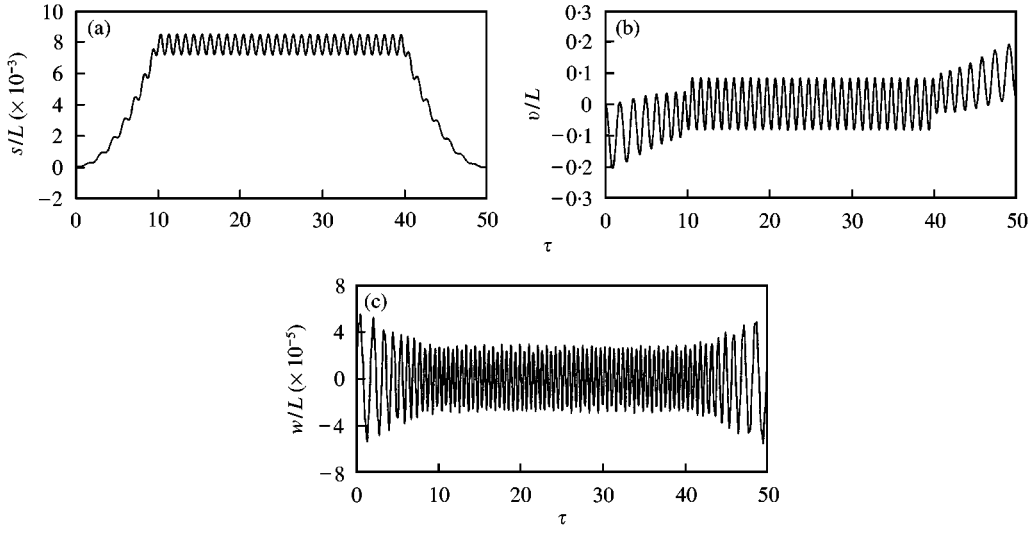

Figure 7. Deformation time histories at $\xi = 1$ for the non-smooth rotating speed profile: (a) the dimensionless stretch deformation s/L; (b) the dimensionless chordwise deformation v/L; and (c) the dimensionless flapwise deformation w/L.

When the rotating speed is constant, the periods of the chordwise and flapwise vibrations are closely related to the first natural frequencies for the chordwise and flapwise motions. Scrutinize the time responses during $10 \leqslant \tau \leqslant 40$ when the rotating speed is constant. The oscillations for the chordwise motion during the interval, as shown in Figures 6(a), 6(b), 7(a) and 7(b), have an average dimensionless period of 1·0017, while the oscillations for the flapwise motion, as shown in Figures 6(c) and 7(c), have a period of 0·5299. From these periods, the first dimensionless natural frequencies for the chordwise and flapwise motions are computed as 6·2725 and 11·8573 respectively. When $\delta = 0{\cdot}1$, $\alpha = 70$ and $\gamma = 10$, the first dimensionless natural frequencies, which are read out from Figure 4 are 6·2726 for the chordwise motion and 11·8578 for the flapwise motion. Hence the first natural frequencies can be obtained from the time responses when the rotating speed is constant.

Denoting the stretching, the chordwise bending, and the flapwise bending stresses by σ_s, σ_v and σ_w, respectively, the maximum values of the stresses are given by

$$\sigma_s = E\frac{\partial s}{\partial x}, \quad \sigma_v = -\frac{EB}{2}\frac{\partial^2 v}{\partial x^2}, \quad \sigma_w = -\frac{EH}{2}\frac{\partial^2 w}{\partial x^2}, \tag{51}$$

where B and H are the width and height of the beam. Substituting equation (28) into equation (51), the stresses in an element can be expressed in terms of the nodal degrees of freedom of s_e, v_e, θ_e, w_e,ψ_e, s_{e+1}, v_{e+1}, θ_{e+1}, w_{e+1} and ψ_{e+1}:

$$\sigma_s = E\frac{s_{e+1} - s_e}{h_e}, \tag{52}$$

$$\sigma_v = -\frac{EB}{h_e^2}\left[\frac{3(v_e - v_{e+1})(2x - x_e - x_{e+1})}{h_e} + \theta_e(3x - x_e - 2x_{e+1}) + \theta_{e+1}(3x - 2x_e - x_{e+1})\right], \tag{53}$$

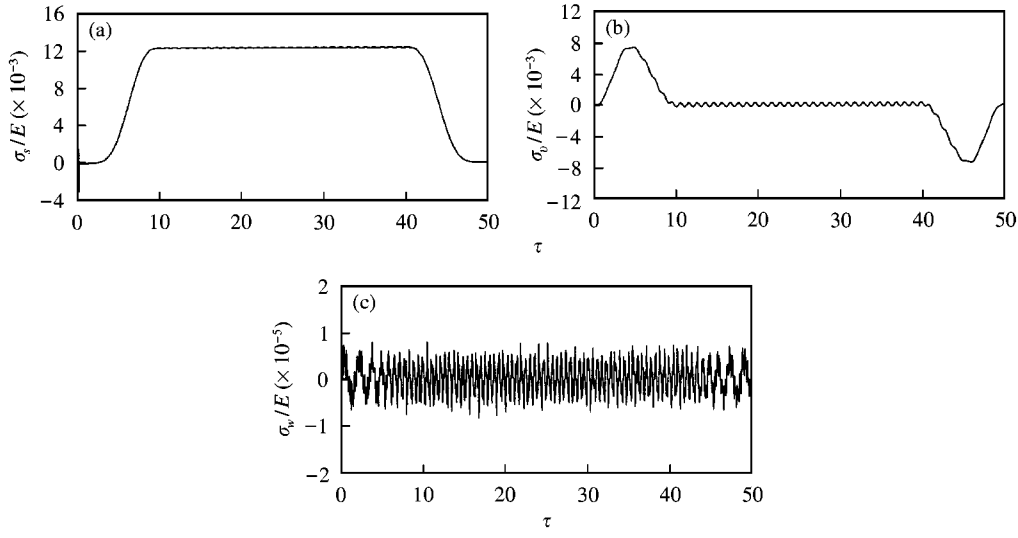

Figure 8. Stress time histories at $\xi = 0$ for the smooth rotating speed profile: (a) the dimensionless stretching stress σ_s/E; (b) the dimensionless chordwise bending stress σ_v/E; and (c) the dimensionless flapwise bending stress σ_w/E.

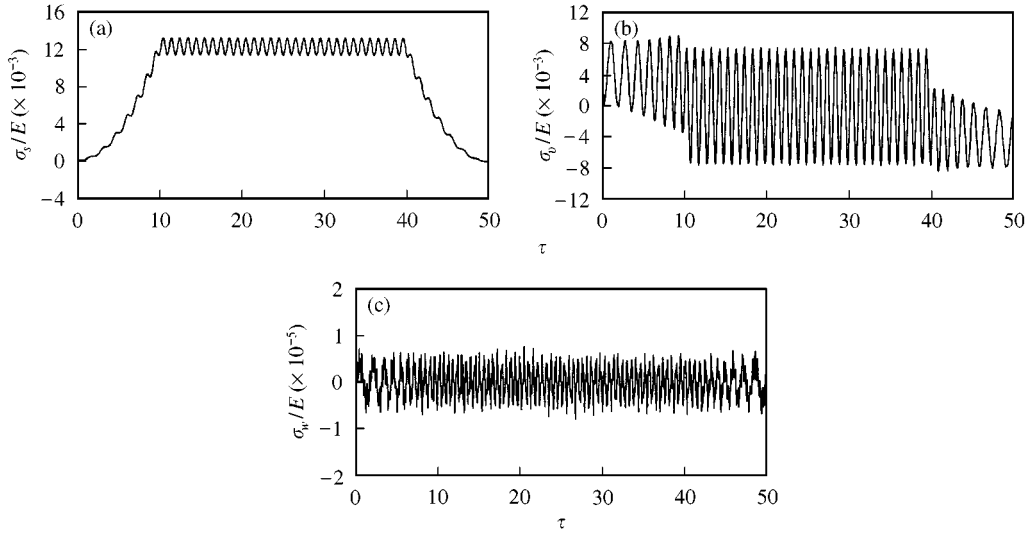

Figure 9. Stress time histories at $\xi = 0$ for the non-smooth rotating speed profile: (a) the dimensionless stretching stress σ_s/E; (b) the dimensionless chordwise bending stress σ_v/E; and (c) the dimensionless flapwise bending stress σ_w/E.

$$\sigma_w = -\frac{EH}{h_e^2}\left[\frac{3(w_e - w_{e+1})(2x - x_e - x_{e+1})}{h_e} + \psi_e(3x - x_e - 2x_{e+1}) + \psi_{e+1}(3x - 2x_e - x_{e+1})\right]. \tag{54}$$

Time histories of the stresses can be obtained by using equations (52)–(54), once the deformations are computed from equations (37) and (40). Since the stress of a cantilever

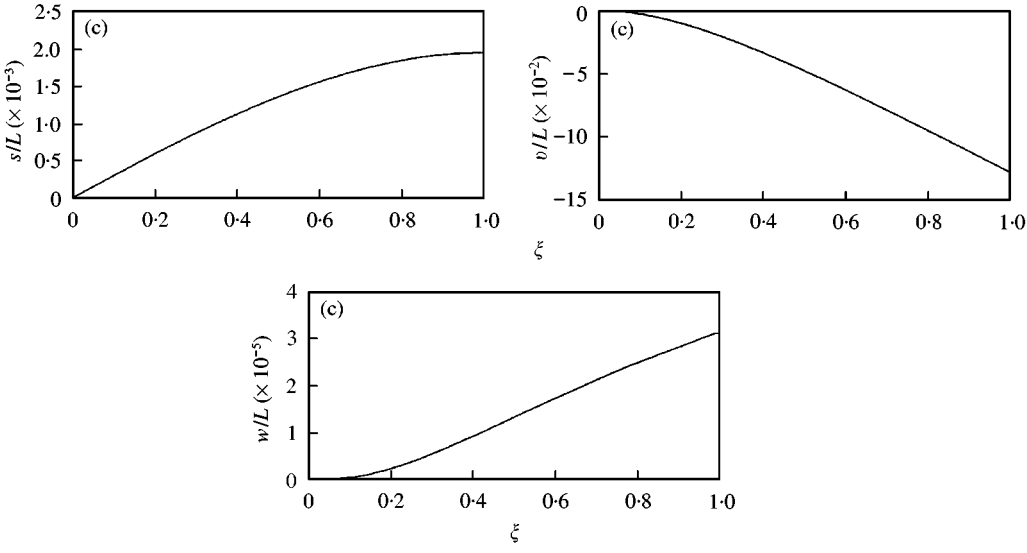

Figure 10. Deformation distributions at $\tau = 5$ for the smooth rotating speed profile: (a) the dimensionless stretch deformation s/L; (b) the dimensionless chordwise deformation v/L; and (c) the dimensionless flapwise deformation w/L.

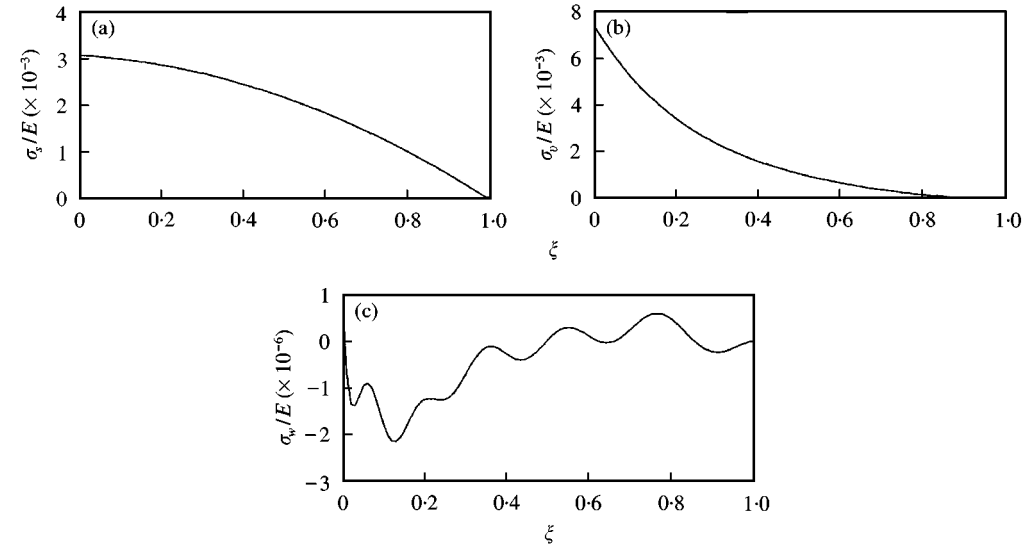

Figure 11. Stress distributions at $\tau = 5$ for the smooth rotating speed profile: (a) the dimensionless stretching stress σ_s/E; (b) the dimensionless chordwise bending stress σ_v/E; and (c) the dimensionless flapwise bending stress σ_w/E.

beam is generally maximum at the fixed end, the time responses of the stresses are computed at this end, namely, at $\xi = 0$. Figures 8(a), 8(b), 9(a) and 9(b) illustrate that the time histories of the stretching and chordwise bending stresses for the non-smooth rotating speed profile have larger oscillations than those for the smooth speed profile. This phenomenon occurs in the time histories of the deformation, as shown in Figures 6(a), 6(b), 7(a) and 7(b). However, in Figures 8(c) and 9(c), it is difficult to find a difference between the flapwise bending stresses with the smooth and non-smooth speed profiles.

Finally, the distributions of the deformations and stresses are investigated when the rotating speed of the beam changes with the smooth speed profile defined by equation (48). The distributions are computed when $\tau = 5$, that is, when $\gamma = 5$ and $\lambda = 2$. In this condition, the rotating beam has a positive angular acceleration which yields the inertia effect in the tangential direction. As shown in Figure 10, the magnitudes of all the deformations are zero at the fixed end or at $\xi = 0$, increase with ξ, and become the maximum at the free end or at $\xi = 1$. In fact, the deformation distributions are similar to the first mode shapes of the deformations for the stationary cantilever beam. Accordingly, it is reasonable that in Figure 10(b) and 10(c) the slopes of the chordwise and flapwise deformations are zero at the fixed end. However, the stress distributions plotted in Figure 11 show that the stretching and chordwise bending stresses have maximum values at the fixed end. This is coincidental with the fact that the stretching and chordwise bending stresses originate from the centrifugal force and the bending moment respectively. Since the impulsive pressure is applied to the beam in the flapwise direction, the distribution of the flapwise bending stress has a more complex pattern compared to those of the stretching and chordwise stresses.

6. CONCLUSIONS

The paper presents a finite element analysis for a rotating cantilever beam. Using the stretch deformation instead of the conventional axial deformation, the linear partial differential equations are derived for a rotating cantilever beam undergoing a prescribed rotating motion. In these partial differential equations, the stretch and chordwise deformations are coupled with each other but the flapwise deformation is not coupled with the other deformations. From the partial differential equations and the associated boundary conditions are derived two weak forms: one is for the chordwise motion and the other is for the flapwise motion. With newly defined two-node beam elements for these motions, the weak forms are spatially discretized and are transformed into matrix–vector equations.

Based upon the matrix–vector equations, numerical investigations are performed not only for the natural frequencies but also for the time responses and distributions of the deformations and stresses. The analysis for the natural frequencies shows that the stretch deformation results in the differences between the chordwise and flapwise motions: the veering phenomena and the divergence instability. It is found from the time responses that the non-smooth profile of the rotating speed incurs larger vibration in the chordwise motion than the smooth one. Therefore, if the beam rotates with a smooth speed profile, a large amount of vibration can be reduced. When the impulsive pressure is applied in the flapwise direction, the vibration amplitudes of the flapwise deformation are dependent on the rotating speed while those of the flapwise bending stress are independent of the speed.

REFERENCES

1. R. SOUTHWELL and F. GOUGH 1921 *British A.R.C. Reports and Memoranda*, *No.* 766. The free transverse vibration of airscrew blades.
2. M. SCHILHANSL 1958 *ASME Journal of Applied Mechanics* **25**, 28–30. Bending frequency of a rotating cantilever beam.
3. S. PUTTER and H. MANOR 1978 *Journal of Sound and Vibration* **56**, 175–185. Natural frequencies of radial rotating beams.
4. H. BAUER 1980 *Journal of Sound and Vibration* **72**, 177–189. Vibration of a rotating uniform beam.
5. S. HOA 1979 *Journal of Sound and Vibration* **67**, 369–381. Vibration of a rotating beam with tip mass.

6. A. WRIGHT, C. SMITH, R. THRESHER and J. WANG 1982 *ASME Journal of Applied Mechanics* **49**, 197–202. Vibration modes of centrifugally stiffened beams.
7. Y. KUO, T. WU and S. LEE 1994 *Computers & Structures* **22**, 229–236. Bending vibration of a rotating non-uniform beam with tip mass and an elastically restrained root.
8. T. YOKOYAMA 1988 *International Journal of Mechanical Sciences* **30**, 743–755. Free vibration characteristics of rotating Timoshenko beams.
9. K. SUBRAHMANYAM, K. KAZA, G. BROWN and C. LAWRENCE 1987 *Journal of Aircraft* **24**, 342–352. Nonlinear vibration and stability of rotating pre-twisted, preconed blades including Coriolis effects.
10. H. H. YOO and S. H. SHIN 1998 *Journal of Sound and Vibration* **212**, 807–828. Vibration analysis of rotating cantilever beams.
11. A. LEISSA 1981 *Applied Mechanics Reviews* **34**, 629–635. Vibration aspects of rotating turbomachinery blades.
12. J. RAO 1987 *Shock and Vibration* **19**, 3–10. Turbomachine blade vibration.
13. H. FRISCH 1975 *NASA TN D*-8047. A vector-dyadic development of the equations of motion for N-coupled flexible bodies and point masses.
14. J. HO 1977 *Journal of Spacecraft and Rockets* **14**, 102–110. Direct path method for flexible multibody spacecraft dynamics.
15. C. BODLEY, A. DEVERS, A. PARK and H. FRISCH 1978 *NASA TP*-1219. A digital computer program for the dynamic interaction simulation of controls and structure.
16. W. HURTY, J. COLLINS and G. HART 1971 *Computers & Structures* **1**, 535–563. Dynamic analysis of large structures of modal synthesis techniques.
17. A. L. HALE and L. MEIROVITCH 1980 *Journal of Sound and Vibration* **69**, 309–326. A general substructure synthesis method for the dynamic simulation of complex structures.
18. T. BELYTSCHKO and B. HSIEH 1973 *International Journal for Numerical Methods in Engineering* **7**, 255–271. Non-linear transient finite element analysis with convected coordinates.
19. J. C. SIMO and L. VU-QUOC 1986 *ASME Journal of Applied Mechanics* **53**, 849–863. On the dynamics of flexible beams under large overall motions—the plane case: parts I and II.
20. E. CHRISTENSEN and S. LEE 1986 *Computers & Structures* **23**, 819–829. Non-linear finite element modelling of the dynamic system of unrestrained flexible structures.
21. H. H. YOO, R. R. RYAN and R. A. SCOTT 1995 *Journal of Sound and Vibration* **181**, 261–278. Dynamics of flexible beams undergoing overall motion.
22. J. CHUNG and G. M. HULBERT 1993 *ASME Journal of Applied Mechanics* **60**, 371–375. A time integration algorithm for structural dynamics with improved numerical dissipation: the generalized-α method.